Geochemistry, Geophysics, Geosystems

RESEARCH ARTICLE
10.1029/2020GC009576

Key Points:

- Off-axis seamounts in segment KR1 of the little-explored Australian-Antarctic Ridge mostly formed within 3 Myrs based on magnetic data
- Simple 2-D magnetic modeling was effective for constraining the off-axis seamount formation period
- Several seamounts formed later than the underlying seafloor were indicative of an extra melting supply in the KR1 region

Correspondence to:
S.-S. Kim,
seungsep@cnu.ac.kr

Citation:
Choi, H., Kim, S.-S., & Park, S.-H. (2021). Magnetic constraints on off-axis seamount volcanism in the easternmost segment of the Australian-Antarctic Ridge. *Geochemistry, Geophysics, Geosystems*, *22*, e2020GC009576. https://doi.org/10.1029/2020GC009576

Received 1 DEC 2020
Accepted 18 AUG 2021

Magnetic Constraints on Off-Axis Seamount Volcanism in the Easternmost Segment of the Australian-Antarctic Ridge

Hakkyum Choi[1], Seung-Sep Kim[2], and Sung-Hyun Park[1]

[1]Division of Earth Sciences, Korea Polar Research Institute, Incheon, Republic of Korea, [2]Department of Geological Sciences, Chungnam National University, Daejeon, Republic of Korea

Abstract The Australian-Antarctic Ridge (AAR) is an intermediate-spreading rate system located between the Southeast Indian Ridge and Macquarie Triple Junction of the Australian-Antarctic-Pacific plates. KR1 is the easternmost and longest AAR segment and exhibits unique axial morphology and various volcanic structures. We identified three asymmetric seamount chains positioned parallel to the seafloor spreading direction, which were indicative of prevalent off-axis volcanism in the vicinity of segment KR1. Two-dimensional magnetic modeling was used to predict the magnetization polarity of the seamounts, as well as to constrain their formation time and duration. The magnetic modeling revealed that the majority of the examined seamounts were formed over a period of less than ~600 kyrs. The seamount formation primarily occurred during two distinct volcanic pulses from 0.16–1.14 to 1.58–2.69 Ma. A temporal gap of 200–650 kyrs between the formation time of the seamounts and seafloor was estimated for certain seamounts that were formed much later than their underlying seafloor and at a distance of 10–20 km from the KR1 axis. Typically, such off-axis seamount activity is related to axial mantle convection caused by excessive magma supply near the ridge crest. Considering the scale of off-axis volcanism and thickening lithosphere ~20 km away from the axis with intermediate-spreading rates, small-scale upwelling made feasible by the fertile mantle heterogeneity is proposed as the mechanism for the seamount formations at off-axis distances, and the geochemically enriched compositions of the seamounts support this alternative explanation.

Plain Language Summary The easternmost spreading center of the Australian-Antarctic Ridge is a plate boundary between the Australian and Antarctic plates, with a large number of underwater volcanoes. The formation time and duration of the underwater volcanic activities were estimated using high-resolution shipboard magnetic data. Some underwater volcanoes appear to have been formed at a considerable distance from the spreading center, which implies the presence of an excessive magma supply. Our analysis on the temporal gap between the underwater volcanoes and their underlying seafloor formations indicated that these volcanoes originated from a non-uniform source of upper mantle.

1. Introduction

Seamounts offer key information to understand various tectonic and volcanic processes occurring in the Earth's lithosphere and the mantle domain beneath (Anderson et al., 2021; Batiza, 1982; Briais et al., 2009; Hwang & Kim, 2016; Koppers & Watts, 2010; Wessel, 1997). At spreading plate boundaries, seamounts tend to be clustered near transform and fracture zones, large overlapping spreading centers, and elevated ridge segments due to anomalously abundant magma supply (Batiza, 1982; Fornari et al., 1988; Reynolds & Langmuir, 2000; Smith & Cann, 1992; Zindler et al., 1984). Most seamounts produced in this tectonic environment are relatively small (<1 km high), while some may continue to grow as they move away with the plate (Anderson et al., 2021; Hillier, 2007; Kim & Wessel, 2011; Watts et al., 2006; Wessel et al., 2010). Such proximity of seamount formation to active spreading centers indicates that the magma supply systems associated with decompression melting of upwelling mantle beneath ridges largely control the formation and growth of the seamounts. Furthermore, the focused distribution of small seamounts can be another important mechanism for oceanic crust accretion, in addition to the generation of crust by seafloor spreading itself (Kim & Wessel, 2011; Wessel, 1997). However, our understanding on the tectonic implications of seamounts is significantly limited by the spatial coverage of available geophysical and geochemical data sets.

Off-axis volcanism is observed at distance ~5 km away from the ridge axis because melt prefers to flow toward the nearby axis (Coumans et al., 2015; Katz et al., 2006). Tectonic conditions modulated with the availability of melt supply, the preferred paths of melting migration, and the variations in spreading rates and ridge migration over the heterogeneous mantle would result in the asymmetric distributions of off-axis seamounts with respect to the ridge (Clague et al., 2000; Coumans et al., 2015; Davis & Karsten, 1986; Fornari et al., 1988; Katz et al., 2006; Scheirer & Macdonald, 1995). Whereas some isolated off-axis seamounts appear to be associated with axial mantle upwelling enhanced by steady-state axial magma chambers and then controlled by the evolution of the axial lithosphere (Scheirer & Macdonald, 1995; White et al., 1998), the short off-axis seamount chains are more related to the magmatism induced by mantle heterogeneities not involving the axial magma plumbing system (Davis & Karsten, 1986; Fornari et al., 1988; Harmon et al., 2011; Wilson, 1992). Davis and Karsten (1986) explained the off-axis seamount chains on the flanks of the Juan de Fuca Ridge (JFR) as being the result of upwelling and early melting of upper mantle heterogeneities, based on the thermal structure models beneath the JFR incorporated with varying ridge migration and mantle heterogeneity. A recent geochemical study on the ~170-km-long 8°20′N near-axis seamount chain in the East Pacific Rise (EPR) revealed the extreme heterogeneity of the near-ridge upper mantle and suggested the presence of sub-seamount plumbing systems separated from the on-axis decompression melting system to prevent any degree of mixing (Anderson et al., 2021). Nonetheless, the geochemical data at off-axis seamounts remain still sparse to constrain global sub-ridge mantle heterogeneities and dating off-axis seamounts to reveal tectonic evolution of off-axis volcanism are even more challenging. More importantly, the current location of the off-axis seamounts mapped in bathymetry is not their birthplace because the seamounts and underlying plate are constantly moving. Without age constraints on off-axis seamounts, the horizontal scale of heterogeneous sub-ridge mantle can be biased.

To constrain temporal evolution of seamount formation, indirect seamount dating using plate flexure modeling (Calmant, 1987; Hwang & Kim, 2016; Kim & Wessel, 2010; Watts et al., 2006; Wessel et al., 2010) or magnetic anomaly analysis (Maia et al., 2005; Sager & Pringle, 1990) is frequently applied because only a small number of seamounts have been dated radiometrically (Briais et al., 2009; Clouard & Bonneville, 2005; Koppers & Watts, 2010; Koppers et al., 2012). Most of these dating efforts are used to investigate hotspot-related large volcanic structures. The recent interdisciplinary expedition on the 8°20′N near-axis seamount chain is also limited to utilize sediment thickness variation determined from the near-bottom chirp data in order to examine age progression of the seamount chain (Anderson et al., 2021; Fabbrizzi et al., 2020).

Here we present magnetically constrained ages of off-axis seamounts located in the vicinity of segment KR1, the eastern end of the Australian-Antarctic Ridge (AAR), using the shipboard magnetic anomalies (Figure 1). These three off-axis seamount chains oriented perpendicular to the ridge provide unique opportunities to constrain the spatial and temporal variation of the off-axis volcanism in the study area (Choi et al., 2021). A 2-D forward magnetic modeling method (Mendel et al., 2005) is used to determine the magnetization polarity sequence of the off-axis seamounts at the time of their formation. In this analysis, we demonstrate that off-axis volcanism can be dated effectively using a few shipboard magnetic survey lines.

1.1. Tectonic Setting

The Australian-Antarctic Ridge (AAR) extends eastward from the Southeast Indian Ridge (SEIR) at around 140°E and ends at the Macquarie Triple Junction (MTJ) of the Australian-Antarctic-Pacific plates at around 161°E (Figure 1). This ~2,000-km-long AAR had not been surveyed with modern shipboard geophysical instruments because of its inaccessibility due to rough sea conditions and remoteness of the area. Recently, Korea-led systematic marine expeditions have investigated the AAR using the R/VIB *Araon*, and these expeditions have yielded significant scientific findings on the hydrothermal activity, tectonic reorganization, and mantle dynamics within this area (Choi et al., 2017; Hahm et al., 2015; Park et al., 2019; Yi et al., 2019). Based on these surveys, the eastern spreading segments of the AAR are named as KR1, KR2, KR3, and KR4, progressing northwestward from the MTJ (Figure 1) (e.g., Choi et al., 2017; Hahm et al., 2015).

Along the SEIR in the Southern Ocean, the most well-known tectonic feature is the Australian-Antarctic Discordance (AAD) located between 115° and 125°E, which has been once proposed as a mantle convection boundary between the Indian and Pacific mantle domains (Hanan et al., 2004; Klein et al., 1988). Although the prominent negative gravity signals and anomalous seafloor roughness of the AAD require more

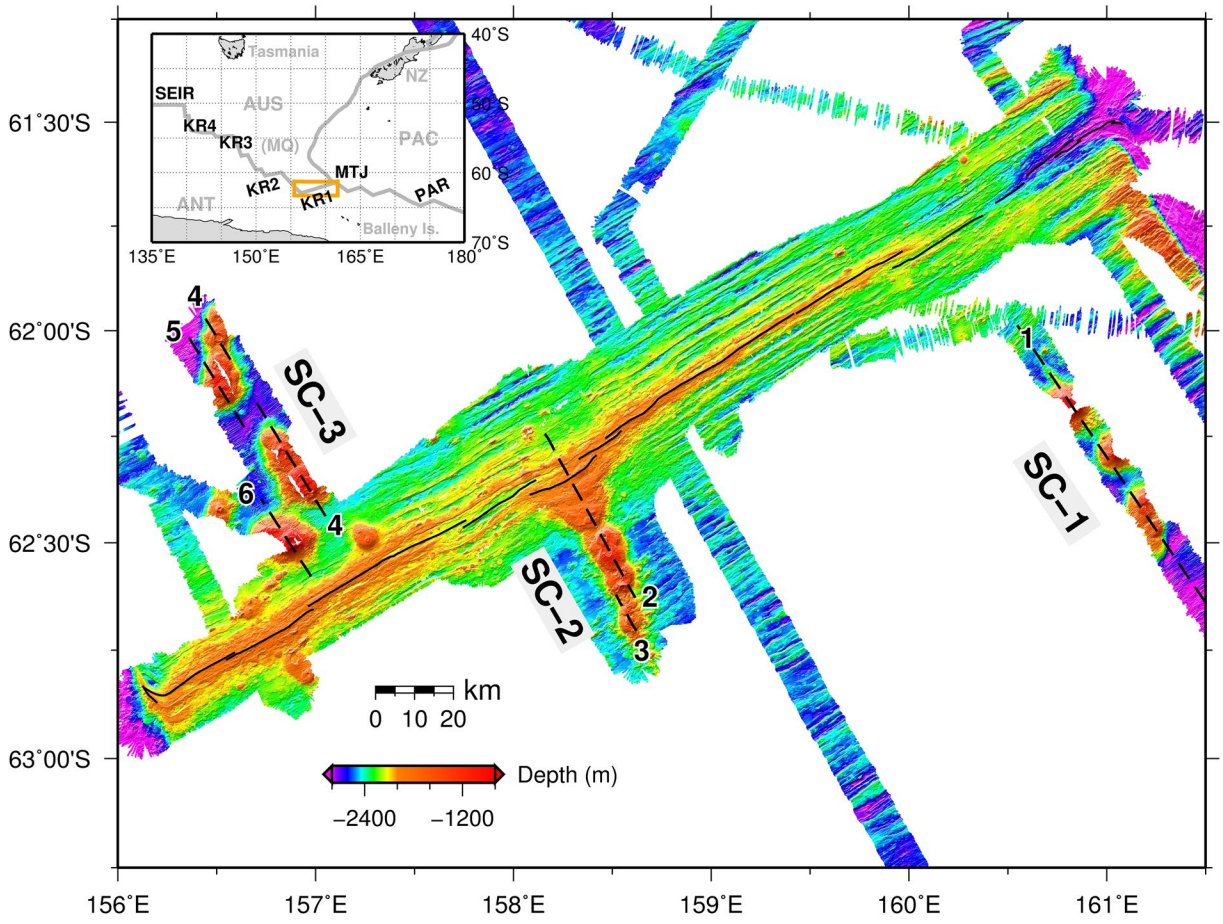

Figure 1. High-resolution bathymetric map of KR1, the first-order segment of the Australian-Antarctic Ridge (AAR) extending from the Macquarie Triple Junction (MTJ) (see the inset). The spreading-axis of KR1 is traced by the black solid lines, whereas the black dashed lines with numbers indicate the shipboard magnetic survey lines crossing over the off-axis seamount chains SC-1, SC-2, and SC-3, respectively. The locations of the AAR, including KR1 and the major tectonic structures near KR1, are shown in the inset map: AUS, Australian Plate; ANT, Antarctic Plate; PAC, Pacific Plate; MQ, Macquarie Plate; SEIR, Southeast Indian Ridge; PAR, Pacific-Antarctic Ridge; MTJ, Macquarie Triple Junction; NZ, New Zealand.

in-depth studies (Christie et al., 1998; Whittaker et al., 2010), the AAD is no longer the boundary between the Indian and Pacific mantle domains (Park et al., 2019). As the sampling gap along the AAR between the AAD and Pacific-Antarctic Ridge (PAR) has been progressively narrowed by our expeditions, the new Zealandia-Antarctic mantle domain is recognized based on the distinct isotopic signature of the AAR basalt samples, exhibiting the similarity with the neighboring volcanic features including Ross Island, the West Antarctic Rift System, Balleny and Scott Islands, and Zealandia, but separable from the Indian and Pacific mantles (Park et al., 2019). Such wide-spread volcanism associated with the Zealandia-Antarctic mantle domain can be unique windows to understand the heterogeneities of the lower and upper mantle in the Southern Ocean. As the AAR is centered in this newly found mantle domain, the off-axis volcanism of the AAR may lead us to constrain sub-ridge mantle heterogeneities modulated by the Zealandia-Antarctic mantle.

The global model for spreading rates, MORVEL (Mid-Ocean Ridge VELocity), indicates that the full-spreading rates of the SEIR reach a maximum of ~70 mm/yr near the AAD and then decrease sinusoidally with the change in angular distance along the plate boundary (DeMets et al., 2010). The full-spreading rates of the AAR vary from ~68 mm/yr near the Tasman Fracture Zone (FZ) at 150°E to ~64 mm/yr at the MTJ (DeMets et al., 2010). In particular, the full-spreading rates of 60–67 and 66–70 mm/yr for segments KR1 and KR2, respectively, were estimated directly from shipboard magnetic data (Choi et al., 2017). According to the classifications of the full-spreading rate (Dick et al., 2003; Macdonald, 2001; Supak et al., 2007), the AAR is an intermediate-spreading ridge with full-spreading rates of 50–80 mm/yr (Choi et al., 2017).

The 300-km-long segment KR1 exhibits a relatively rapid transition from an axial valley in the east to an axial high in the west (Choi et al., 2013; Choi et al., 2021; Kim et al., 2015; Park et al., 2014). Difference in axial morphology is primarily modulated by the thickness of the axial lithosphere, which in turn is controlled by the axial heat flux of magma delivered to the axis (Dick et al., 2003; Macdonald, 2001; Phipps Morgan & Chen, 1993). By examining the Mid-Atlantic Ridge and Juan de Fuca Ridge (JFR), Ito and Behn (2008) showed that the processes related with the frequency and spatial variation of magmatic intrusions and eruptions can influence axial morphology. The coexistence of two end-members in the axial morphology (i.e., the axial valley and high) along segment KR1, and their transition without significant ridge segmentation may imply that the spatial variation of the magma supply system is another pivotal factor in determining the axial morphology of segment KR1, in addition to the spreading rates (Figure 1).

2. Data and Methods

We examined six shipboard magnetic tracks crossing over the off-axis seamounts in the study area (see the dashed lines in Figure 1). The first magnetic surveys for the seamounts near the central KR1 segment were conducted in 2013 (Choi et al., 2013), where seamount chain SC-2 stretches to the southeast from the ridge axis (Lines 2 and 3 in Figure 1). The other seamount chains were surveyed in 2017 as follows: seamount chain SC-1 in the eastern KR1 aligned to the southeast (Line 1) and seamount chain SC-3 in the western KR1 stretching to the northwest (Lines 4, 5, and 6). All the ship tracks were oriented parallel to the direction of seafloor spreading, and the shipboard magnetic data were collected using the marine magnetometer *SeaSpy* (Marine Magnetics Corp., Markham, ON, Canada). The magnetic anomalies were then computed by removing the International Geomagnetic Reference Field (IGRF) model from the observed data (the 12th generation; Thébault et al., 2015).

Magnetic modeling to estimate magnetization characteristics of seamounts, such as polarities of remanent magnetization of the seamount crust, has been performed by a series of inversion and forward modeling estimations (Maia et al., 2005; Parker et al., 1987; Sager & Pringle, 1987). Outcomes from such estimation can provide insights on volcanic processes that formed the seamounts, including constraints on the timing of volcanism (e.g., Maia et al., 2005; Sager & Pringle, 1987). The three-dimensional nature of seamount magnetization due to its crustal formation and evolution over is, however, a hurdle to expand the modeling beyond using a uniformly magnetized body (Maia et al., 2005; Parker, 1988, 1991; Parker et al., 1987; Sager & Pringle, 1987). Maia et al. (2005) attempt to overcome this complexity by deploying well-constrained 3-D nature of the seamounts using full-coverage bathymetry data and sea-surface magnetic profiling perpendicular to the seafloor spreading directions. For our study, however, thoroughly demonstrating the approach by Maia et al. (2005) is challenging because of the limitation of the nature of our data set. We aim to conduct our modeling in two-dimensional manner (e.g., Mendel et al., 2005) enhanced with optimization on interpretation using three-dimensional synthetic models.

To demonstrate our approach, we carried out 3-D magnetic modeling using a synthetic seamount seated on top of a seafloor spread with a full-spreading rate of 60 mm/yr (Figure 2). Following Parker (1973) and Blakely (1995), the Fourier transform ($\mathcal{F}$) of the total magnetic anomaly (ΔT) resulted from a magnetized layer with uneven top $\left(z_1\right)$ and bottom $\left(z_2\right)$ surfaces is given by

$$\mathcal{F}[\Delta T(x,y)] = \frac{1}{2}\mu_0\Theta_{\mathbf{m}}\Theta_{\mathbf{f}}e^{|k|z_0}\sum_{n=1}^{\infty}\frac{(-|k|)^n}{n!}\mathcal{F}[M(x,y)(z_1^n(x,y)-z_2^n(x,y))], \quad (1)$$

where μ_0 is the magnetic permeability of free space, z_0 is the regional depth to the source layer, and $|k|$ is defined by $\left(k_x^2+k_y^2\right)^{1/2}$ with the wavenumbers k_x and k_y in the x and y directions, respectively. Here the magnetization ($\Theta_{\mathbf{m}}$) and ambient field ($\Theta_{\mathbf{f}}$) components are defined as

$$\Theta_{\mathbf{m}} = \hat{m}_z + i\left(\hat{m}_x k_x + \hat{m}_y k_y\right)/|k|$$

and

$$\Theta_{\mathbf{f}} = \hat{f}_z + i\left(\hat{f}_x k_x + \hat{f}_y k_y\right)/|k|$$

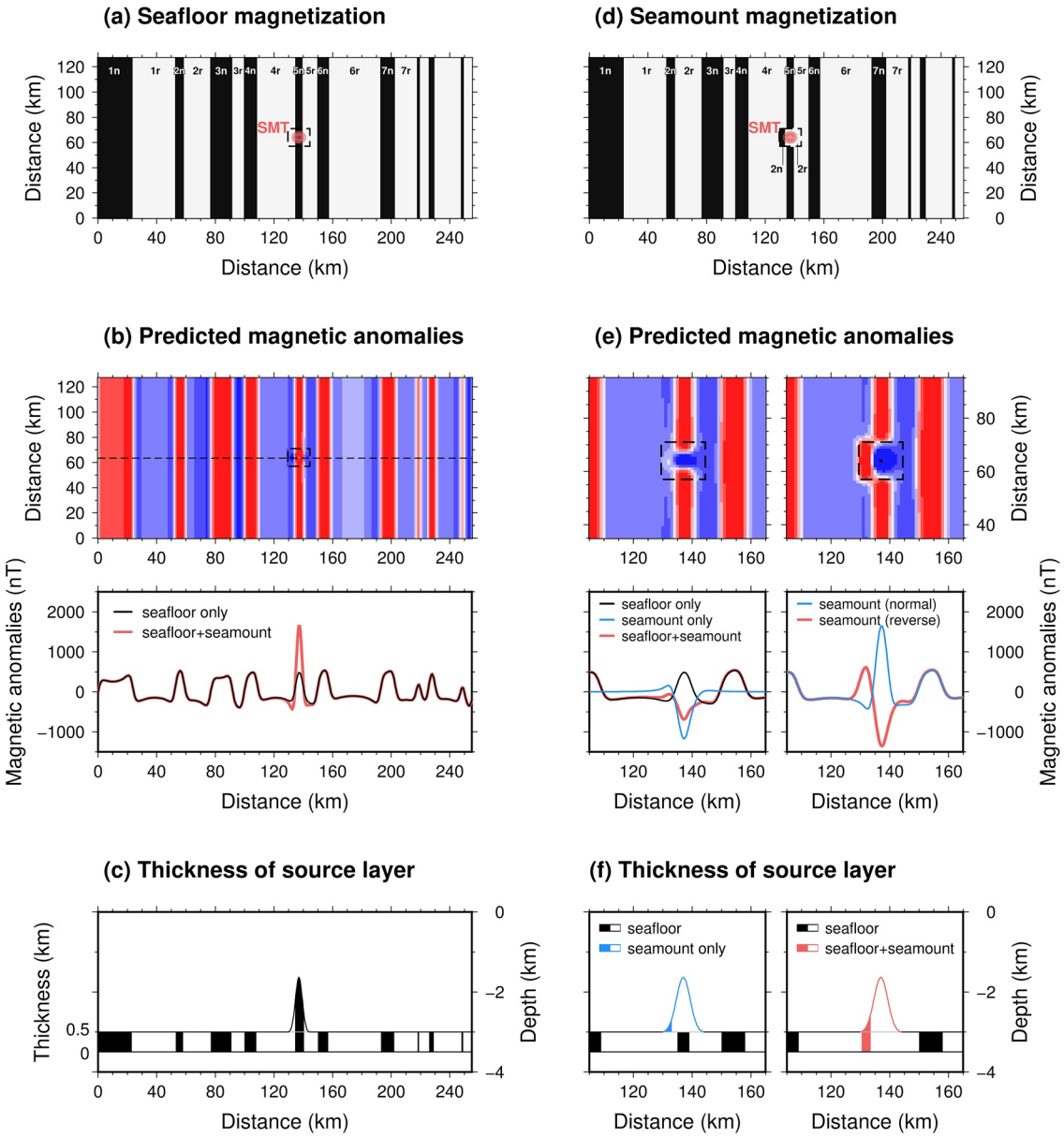

Figure 2. Magnetic modeling for synthetic seafloor and seamount. (a) Seafloor magnetization model converted from the geomagnetic timescale (Cande & Kent, 1995). A synthetic Gaussian seamount is magnetized identical to the seafloor. (b) Predicted magnetic anomalies from the synthetic seafloor spreading model and seamount. Along the dashed line, the magnetic profiles caused by the seafloor spreading model only (black line) and both the seafloor and seamount models (red line) are compared. (c) The thickness of source layer for 3-D magnetic modeling. This synthetic seamount has the same geomagnetic polarity sequence with the seafloor. (d) Seamount magnetized differently from its underlying seafloor. (e) We compare the predicted magnetic anomalies with different source layers, as shown in (f). Although the magnetic anomaly amplitude can differ due to thickness variation in source layer, the anomaly shape resulted from the seamount magnetization is persistent for both cases.

where $i = \left(-1\right)^{1/2}$. $\hat{\mathbf{m}}$ and $\hat{\mathbf{f}}$ are the unit vectors parallel to the magnetization and ambient fields, respectively. If z_1 and z_2 are both constant, Equation 1 can be further simplified (Blakely, 1995). In addition, Equation 1 can be solved iteratively after isolating the $n = 1$ term to image the distribution of seafloor and seamount magnetization (Caratori Tontini et al., 2008; Parker & Huestis, 1974).

For the synthetic seafloor-spreading magnetic anomalies, we first converted the geomagnetic timescale (Cande & Kent, 1995) to the distance by multiplying the given timescale and half-spreading rate (Figures 2a and 2d). Then the seafloor was assumed to be situated at 3 km depth with a flat topography (i.e., z_1 and z_2 are

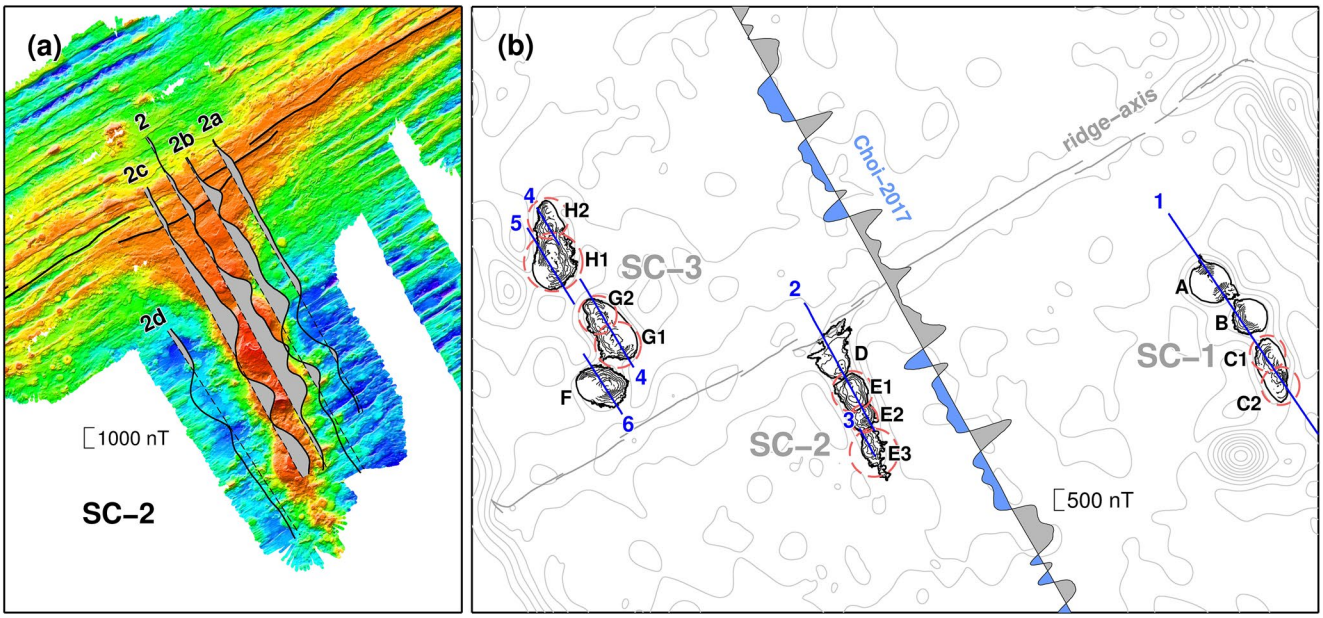

Figure 3. Shipboard magnetic profiles at off-axis seamounts in the study area. (a) Wiggle plot of the magnetic profiles running parallel with the seamount chain SC-2, superimposed on the shipboard bathymetry. The magnetic data from Lines 2a, 2b, 2c, and 2d consistently showed the geomagnetic reversal patterns, whereas Line 2 crossing the center of SC-2 seamounts exhibited a poor correlation with the nearby survey lines. (b) The magnetic profiles acquired at the KR1 seamounts (blue solid lines). Line 3 crossing seamount E3 is the subset of Line 2c shown in Figure 2a. The magnetic profile across the ridge axis (Choi et al., 2017), far away from any seamounts in the study area, is illustrated by gray and light-blue colors representing positive and negative magnetic anomalies, respectively. The seamounts examined in this study were alphabetically labeled over the satellite-derived bathymetric data at 200 m contour intervals (version 18.1; Smith & Sandwell, 1997). The basal areas of the seamounts exhibiting multiple peaks are denoted by red dashed circles, based on visual inspection.

both constant). The magnetized layer was set as 0.5 km of constant thickness and 10 A/m of uniform magnetization (Dyment & Arkani-Hamed, 1995), assuming there are no significant changes in magnetization for the on-axis (Brunhes period) and off-axis blocks. The magnetization vector was assumed to be parallel to the current geomagnetic field in the vicinity of segment KR1. The geomagnetic reversals were then computed by flipping signs of the given magnetization. As shown in Figure 2b, the magnetic anomalies predicted from the synthetic seafloor exhibited typical geomagnetic reversal patterns similar to the observed data in the study area (Figure 3). Then, we placed a synthetic Gaussian seamount of height 1.5 km and radius 7 km, centered at magnetic anomaly 5n (Figure 2a), by assuming the seamount was magnetized at the same time with the underlying seafloor. The magnetic anomaly resulting from both the seafloor and seamount (red profile in Figure 2b) was larger than the seafloor anomaly (black profile in Figure 2b) at the seamount, because the thickness of magnetized source layer was maximized beneath the seamount (Figure 2c).

To consider the synthetic seamount magnetized differently from its underlying seafloor, we used the younger geomagnetic sequence for the given seamount (Figure 2d). First, we computed the seafloor and seamount magnetic anomalies separately (see black and blue profiles in Figure 2e) and then summed these estimates to form the corresponding synthetic magnetic anomalies. Because the seamount magnetic anomaly was larger than the seafloor spreading magnetic anomaly, the younger geomagnetic sequence assigned to the synthetic seamount was recognizable from the summed magnetic profile (red profile in Figure 2e). We also considered another case that the seafloor was entirely re-magnetized by the seamount magnetization (see right panel in Figure 2f), resulting an increased magnetic anomaly amplitude with the same shape. Both examples illustrated that the geomagnetic sequence recorded at a seamount could be distinguishable from the seafloor spreading magnetic anomaly in two-dimensional data. Although the amplitude of seamount magnetic anomaly would depend on the degree of re-magnetized seafloor, the shape of seamount magnetic anomaly was not significantly changed for both cases. Therefore, the difference between the seafloor and seamount magnetic polarity sequences can be identified in this two-dimensional data analysis using magnetic profiles acquired along seafloor spreading direction.

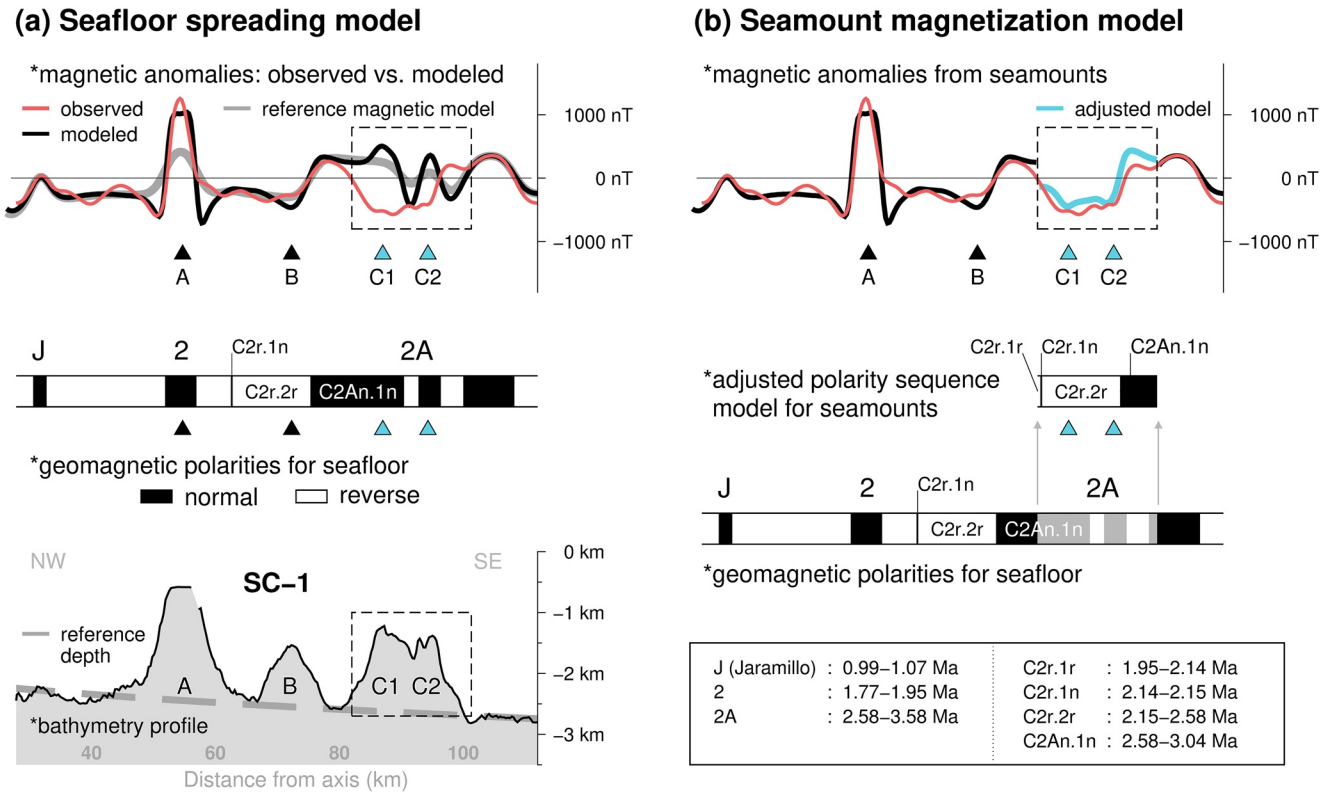

Figure 4. Magnetic modeling for seamounts A, B, C1, and C2 of the seamount chain SC-1. (a) The observed (red line; Figures 1 and 3), modeled (black line), and reference magnetic anomalies (gray line) are compared in the top panel. Both the modeled and reference magnetic anomalies were computed based on the geomagnetic polarities of the SC-1 seafloor (middle panel; Figure 3b). The former takes account of the observed bathymetric profile, whereas the latter uses the reference depth profile (gray dashed line in the bottom panel), which is proportional to the square root of seafloor age. The similarity between these anomalies at seamounts A and B appeared to be associated with the coeval formation of the seamounts and their underlying seafloor. However, at seamounts C1 and C2, we found discrepancies between the observed and predicated data. (b) To minimize the given discrepancies (cyan line), we adjusted the geomagnetic reversal sequence for the seamounts (dotted box area) younger than those of the underlying seafloor (middle panel). The adjusted polarity sequence was used to constrain the formation periods of seamounts C1 and C2 (cyan triangles), whereas the sequence for seafloor spreading was utilized for seamounts A and B (black triangles).

In this study, our prime interest is to estimate for each KR1 seamount whether it was formed during a normal or reversed polarity period, because such information can be used to compute age offset between seamount formation and seafloor age. We first examined the contributions from the underlying oceanic crust to the observed magnetic anomalies. Figure 3a shows the closely spaced short magnetic profiles obtained along seamount chain SC-2. The comparison of these profiles indicated that the magnetic data acquired near to the seamounts were barely affected by the seamount magnetization as the magnetization polarities of Lines 2a, 2b, 2c, and 2d exhibited good correlations with each other and the ridge-crossing profile (Figure 3b). In particular, Lines 2b and 2c crossing over the flanks of seamounts D and E1 still exhibited the transition from magnetic anomaly 1 (Brunhes) to C1r.1r and then C1r.1n (Jaramillo) (Cande & Kent, 1995). However, the magnetic profiles crossing the center of the seamounts in the D and E groups (Line 2 and the southern part of Line 2c) were distinctly different from the other nearby magnetic survey lines, thereby indicating that the magnetic anomalies from the underlying seafloor may be overprinted by those from the seamounts as expected.

As demonstrated using the synthetic examples, the shape difference between the observed and seafloor-spreading magnetic anomalies can be regarded as an indicator that the seamount was formed during a different magnetization polarity sequence from the underlying seafloor. This approach is effective because the spreading-parallel magnetic profiles ideally record the polarity sequence of 2-D magnetized bodies. Figure 4 compares the observed magnetic data (red) with the seafloor spreading model (black) along Line 1 at the SC-1 seamounts (Figures 1 and 3). For computing magnetic anomalies resulting from the given seafloor

Table 1
Estimated Magnetic Age of Off-Axis Seamounts Distributed Along KR1

Seamount label		Distance from axis to seamount summit (km)	Estimated age by magnetic model (summit age[a]) (Ma)
A		54.7	1.58–2.11 (1.86)
B		72.3	2.32–2.62 (2.48)
C	C1	87.0	2.12–2.47 (2.30)
	C2	94.3	2.47–2.69 (2.53)
D		12.0	0.00–0.57 (0.46)
E	E1	21.3	0.16–0.55 (0.35)
	E2	30.8	0.55–0.72 (0.65)
	E3	40.0	0.87–1.14 (1.05)
F		16.4	0.27–0.71 (0.46)
G	G1	26.7	0.30–0.57 (0.38)
	G2	37.9	0.57–0.88 (0.72)
H	H1	60.0	1.64–2.14 (1.85)
	H2	72.3	1.62–2.07 (1.82)

[a]The ages in parentheses were determined at the center of the corresponding seamount summit.

spreading model, we utilized the magnetic forward modeling tool, MODMAG (Mendel et al., 2005) and followed Choi et al. (2017)'s definition regarding the geomagnetic timescale (see the middle panel in Figure 4a), which was based on that of Cande and Kent (1995). The MODMAG tool computes seafloor magnetic anomalies using a collection of magnetized rectangular layers and identifies magnetic boundaries based on the user-defined spreading parameters (Mendel et al., 2005).

For the SC-1 seafloor, we used the shipboard bathymetry (see the bottom panel in Figure 4a) and a spreading rate of ~60 mm/yr (Choi et al., 2017). To compute the seafloor spreading magnetic anomalies, we assumed 0.5 km of constant thickness for the magnetized layer, and 19 A/m of magnetization for the on-axis blocks (Brunhes period), ±8 A/m of magnetization for the off-axis blocks to obtain the reasonable amplitudes of the predicted anomalies compared with the observed. The higher magnetization intensity for Brunhes period was needed to account for the most recently placed magnetic source (Mendel et al., 2005; Schouten et al., 1999). The MODMAG tool also utilizes contamination coefficient, which accommodates possible effects due to off-axis intrusions or lava flows covering a significant distance horizontally that might overprint the pre-exiting seafloor magnetic polarity (Mendel et al., 2005). Because such cases are considered mostly for slow-spreading ridges, we used 0.8 of the contamination coefficient (1 for no contamination). Lastly, the magnetization vector was assumed to be parallel to the current geomagnetic field given by the IGRF model (Thébault et al., 2015).

We found the seafloor spreading model exhibited a good correlation with the observed magnetic data even at seamounts A and B (Figure 4a). As the seafloor spreading anomalies (black line) were computed with the observed bathymetric profile (see the bottom panel in Figure 4a), one might consider that the topographic changes at the given seamounts would result in such amplitude variations. To examine possible topographic effects (i.e., changes in distance between the observation points and magnetized bodies) on magnetic anomalies, we computed the reference magnetic anomalies (gray solid line in Figure 4a) using MODMAG with the reference depth profile (gray dashed line in the bottom panel), predicted based on the half-space cooling model of oceanic lithosphere (Parsons & Sclater, 1977). Because the other model parameters were assumed to be the same as those for the seafloor spreading model (black solid line), the reference magnetic anomalies (gray solid line) only reflect the effects of magnetic boundaries, not any topographic changes including seamounts. At seamounts A and B, the reference magnetic anomalies themselves were capturing most of the variation of the observed magnetic anomalies, which indicates that the geomagnetic polarity sequence is a crucial factor for obtaining the best-fit shape when spreading-parallel magnetic profiles are considered.

Furthermore, the observed, modeled, and reference magnetic anomalies at seamounts A and B coincided with each other. Among the model parameters assumed for computing these anomalies, magnetization polarity was the only parameter to change the shape of the anomalies. However, we did not find any evidence indicating that the magnetization vector for these off-axis seamounts had significantly different inclination and declination from the seafloor magnetization. From such consistency in shape among the magnetic anomalies at seamounts A and B, we could infer that the seamounts A and B were formed within the same geomagnetic polarities associated with the underlying seafloor formation. This result also coincided with the synthetic examples considering the coeval formation of the seafloor and seamount, as shown in Figure 2b.

By approximating seamount magnetization as a collection of magnetized 2-D layers exhibiting horizontal age progression assigned by the geomagnetic polarity sequence, we were able to constrain the formation periods of the seamounts based on the polarity sequence model. As for seamount A, for example, we predicted the corresponding formation period as 1.58–2.11 Ma by projecting its width to the geomagnetic polarity sequence (Figure 4 and Table 1). As the polarity sequence used here is based on the geomagnetic timescale having a precision of 10 kyrs (Cande & Kent, 1995), the age bounds estimated for the seamount formation

have the same precision. As for seamount B, however, the similarity between the observed and predicted anomalies might have been obtained because the given ship track did not cross the center of the seamount (Figures 1 and 3b). Although seamount B might have been formed earlier than its underlying oceanic crust, we reserved our prediction to the seafloor age, which is the oldest age constrained for any seamount.

As for seamounts C1 and C2, the seafloor and reference magnetic anomalies (black and gray solid lines in Figure 4a, respectively) failed to reproduce the observed data with the given geomagnetic polarities. Considering seamounts A and B, we characterized that such discrepancy in shape resulted from an offset in geomagnetic polarities between the seamount and seafloor formation periods. Because seamounts can be situated only on the existing seafloor, off-axis seamounts formed with a geomagnetic polarity sequence earlier than that of its underlying seafloor would produce different magnetic anomalous patterns from the seafloor spreading model, as demonstrated with the synthetic examples above (Figure 2e). To find the best polarity sequence for the given seamounts using MODMAG, we considered a seamount as a new seafloor formed on top of the original oceanic crust, which approximates the given seamount as a 2-D horizontal layer of uniform magnetization. Then, we progressively slid the magnetization polarity sequence defined by the spreading rate for the SC-1 seafloor toward the younger period until the shape of the adjusted magnetic anomalies matched with the observed (cyan line in Figure 4b). Here the shifting was carried out in a step size of 10 kyrs, the precision of the geomagnetic timescale used for magnetic modeling (Cande & Kent, 1995). The shifted magnetization polarity was applied only to the seamount area (dotted box area in Figure 4). The optimized polarity sequence was used to constrain the formation period of seamounts C1 and C2 (Figure 4b and Table 1).

In the above modeling, we assumed that the observed magnetic anomalies predominantly originated from remanent magnetization for both seafloor and seamounts (Maia et al., 2005; Mendel et al., 2005; Schouten et al., 1999). The detailed seamount paleopole study showed that viscous and induced magnetizations would contribute to up to 15%–25% of the total magnetization of seamounts (Gee et al., 1993). Such contribution, however, would be mainly due to intrusives. The KR1 seamounts investigated in this study are relatively small (heights <1.5 km) and hence the volumetric contribution of such intrusives may be less compared to large-scale seamounts (e.g., La Palma Seamount; Gee et al., 1993). Therefore, the viscous and induced magnetizations can be less effective for the KR1 seamount magnetization.

From the SC-1 and synthetic seamounts, we demonstrated that a 2-D magnetic modeling approach is effective not only to approximate the observed magnetic anomalies at the seamounts, but also to estimate their formation time. The shipboard magnetic anomalies collected in this study run along the spreading direction and mostly cross over the center of the seamounts, which in turn tend to maximize the 2-D properties of seamount magnetization in modeling. Because the study area consists of a relatively young seafloor (<6 Ma), there are limited possibilities for choosing the optimal seamount polarity from the entire polarity sequences of the seafloor. Thus, we systematically apply the following approach to the seamounts populated near segment KR1: (a) comparison of the observed magnetic anomalies with the seafloor spreading model based on Choi et al. (2017) to assess the degree of discrepancies at seamounts, (b) minimization of the discrepancies, if any, between the observed and predicted anomalies by adjusting the geomagnetic polarity sequence at the given seamounts, and (c) determination of the formation period of the corresponding volcanic event based on the adjusted geomagnetic polarity sequence. As our objective is to estimate the polarity sequence of seamount volcanism, the other model parameters (e.g., magnetization intensity) are not optimized. In the following sections, we present the magnetic estimates on seamount ages and discuss their implications for the off-axis volcanism near segment KR1 of the Australian-Antarctic Ridge, as well as the limitations of our modeling approach.

3. Results

For the SC-1 seamounts, as discussed above, seamounts A and B were constrained by the geomagnetic polarity sequence of the seafloor spreading model (Choi et al., 2017). Using the peak locations, seamounts A and B were dated as 1.86 and 2.48 Ma, respectively (Table 1). As for seamount B, the ship did not cross its center (Figures 1 and 3b), and hence the observed data may reflect the mixed effects from the seafloor and seamount magnetization. Because the given data coverage was not appropriate for isolating the seamount

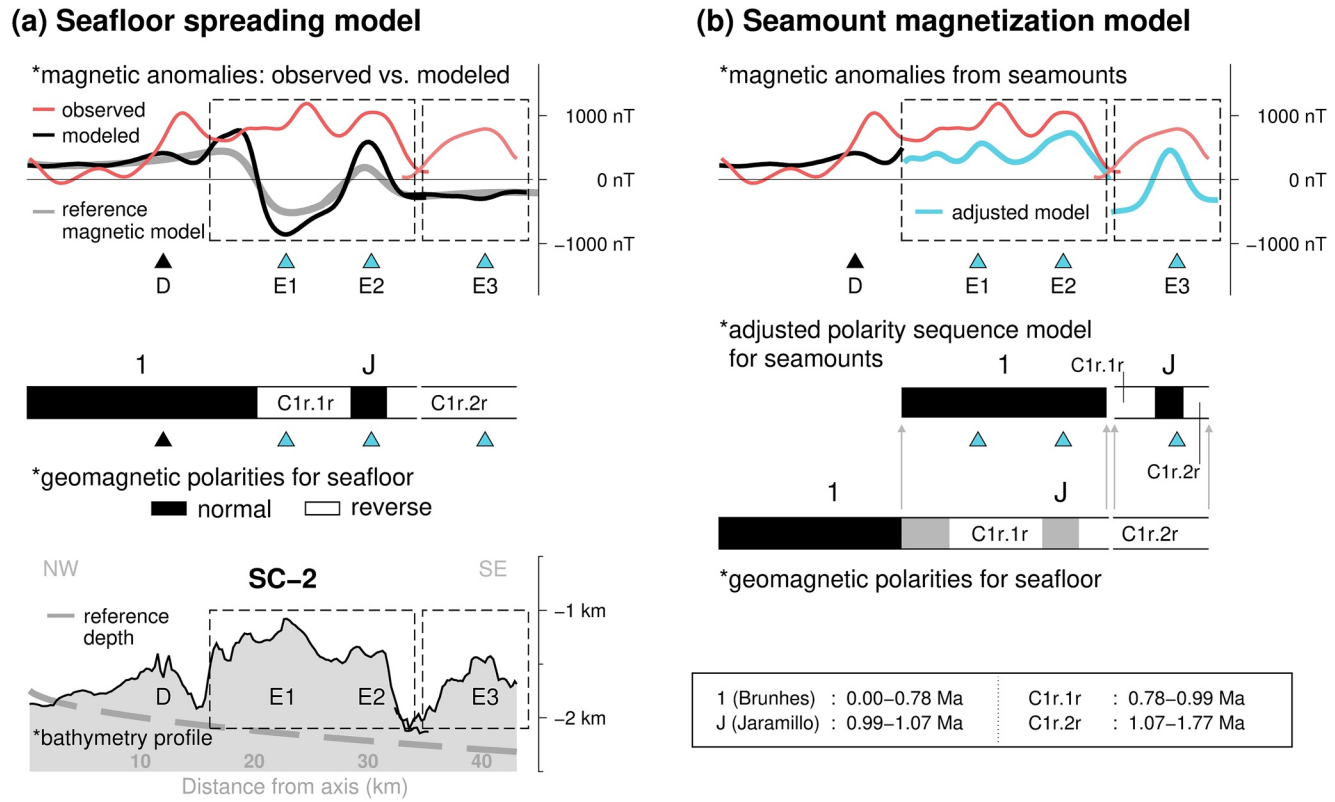

Figure 5. Magnetic modeling for seamounts D, E1, E2, and E3 along the seamount chain SC-2. The geomagnetic polarity sequences for seamounts E1, E2, and E3 were adjusted to minimize the discrepancies between the observed and predicted data. A detailed description can be found in the caption of Figure 4 and the main text.

contribution from the seafloor, we made a conservative prediction for seamount B by choosing the underlying seafloor age although seamount B might have been formed earlier than the estimated. The seafloor model beneath seamounts C1 and C2 estimated as ~3 Ma (Figure 4) was needed to be adjusted to minimize the discrepancies between the observed and predicted data. We found that a temporal gap of ~650 kyrs between the seamount and seafloor formation periods was sufficient to reproduce the observed magnetic anomalous patterns (cyan line in Figure 4b). Thus, seamounts C1 and C2 were dated to approximately 2.12–2.69 Ma (Figure 4b and Table 1). Based on these estimates, we also predicted that seamounts C1 and C2 initially formed approximately ~20 km away from the KR1 axis, but these are currently situated at ~90 km away from the axis.

For the SC-2 seafloor, we used a spreading rate of ~64 mm/yr as segment KR1 has been spreading faster as moving away from the rotation axis of the Macquarie Plate (Choi et al., 2017). For the seafloor beneath seamounts D, E1, E2, and E3, we assumed 14 A/m of magnetization for the on-axis blocks, ±8 A/m of magnetization for the off-axis blocks, and 0.8 for the contamination coefficient for MODMAG computations. The comparative analysis for the SC-2 seamounts first dated seamount D as 0.46 Ma based on the seafloor age, although there was the discrepancy between the observed and predicted anomalies (Figure 5). Because seamount D is situated on the youngest seafloor, no geomagnetic polarity sequence earlier than the seafloor age was considered. The observed magnetic anomalies at seamount D may reflect the geomagnetic excursions during the Brunhes chron (Yang et al., 2007) or variations in the geomagnetic paleo-intensity of the Brunhes chron (Macrì et al., 2010), which will require in-situ samples for further verification. For seamounts E1, E2, and E3, the underlying seafloors were estimated as 0.57–0.95, 0.95–1.10, and 1.16–1.46 Ma, respectively, which in turn resulted in large discrepancies between the observed and predicated data (Figure 5a). Such discrepancies were resolved by adjusting the polarity sequences for seamount E1 as 0.16–0.55 Ma, for seamount E2 as 0.55–0.72 Ma, and for seamount E3 as 0.87–1.14 Ma, respectively (Figure 5b and Table 1). These results required a temporal gap of 300–400 kyrs between the seamount and seafloor formation

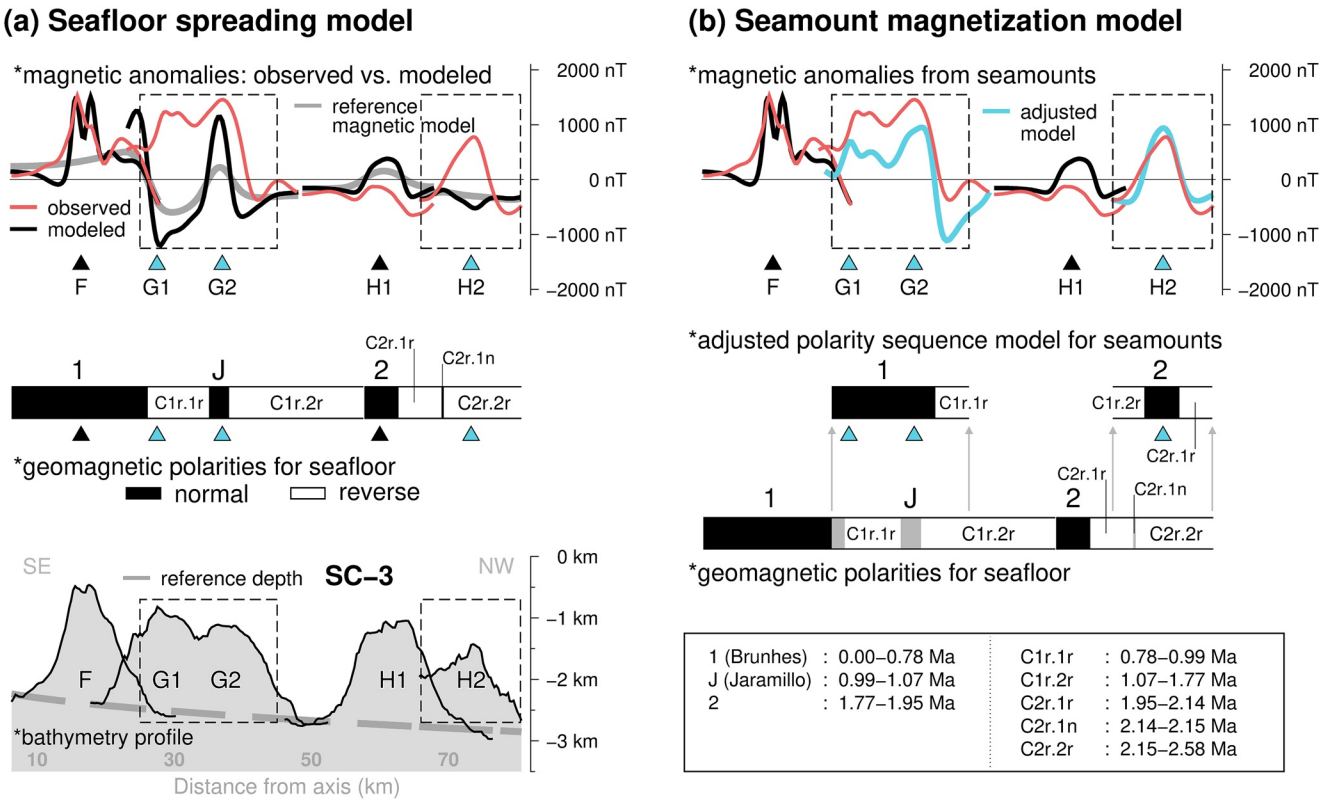

Figure 6. Magnetic modeling for seamounts F, G1, G2, H1, and H2 along the seamount chain SC-3. The geomagnetic polarity sequence for seamounts G1, G2, and H2 were adjusted to minimize the discrepancies between the observed and predicted data. A detailed description can be found in the caption of Figure 4 and the main text.

periods. Consequently, seamounts E1, E2, and E3, which are currently situated between 20 and 40 km from the axis, were estimated to have originally formed approximately ~10 km from the axis. For a better presentation, we applied 18 A/m of magnetization for the on-axis blocks and ±10 A/m of magnetization for the off-axis blocks for seamounts E1 and E2 (Figure 5b), which only affected the level of the predicted anomalies, not their shape.

For the SC-3 seafloor (Figure 6), we used a spreading rate of ~67 mm/yr (Choi et al., 2017), 18 A/m of magnetization for the on-axis blocks, ±11 A/m of magnetization for the off-axis blocks, and 0.8 for the contamination coefficient for MODMAG computations. The comparative analysis required adjustments of the geomagnetic polarity sequences at seamounts G1, G2, and H2. As for seamounts G1 and G2, the temporal adjustments of 300–400 kyrs resulted in a seamount formation period of 0.30–0.88 Ma (Figure 6b and Table 1). Seamount H2 was dated as 1.62–2.07 Ma, with a temporal adjustment of ~400 kyrs from its underlying seafloor. Based on these analyses, seamounts G (G1 and G2) and H2 were estimated to have initially formed ~14 and ~13 km away from the ridge axis, respectively. As for seamounts F and H1, the seafloor age was used for dating their formation periods (Table 1).

Figure 7 summarizes the geomagnetically estimated ages of the off-axis seamounts in the study area. The seamounts depicted in the same color as the underlying seafloor were formed within the same geomagnetic period as the seafloor (e.g., seamounts A and F), whereas the seamounts that required temporal adjustments in the geomagnetic polarity sequence from their underlying seafloor were illustrated in different colors (e.g., seamounts C1 and H2). In the following section, we further discuss the spatial and temporal variations in off-axis volcanism in the vicinity of segment KR1.

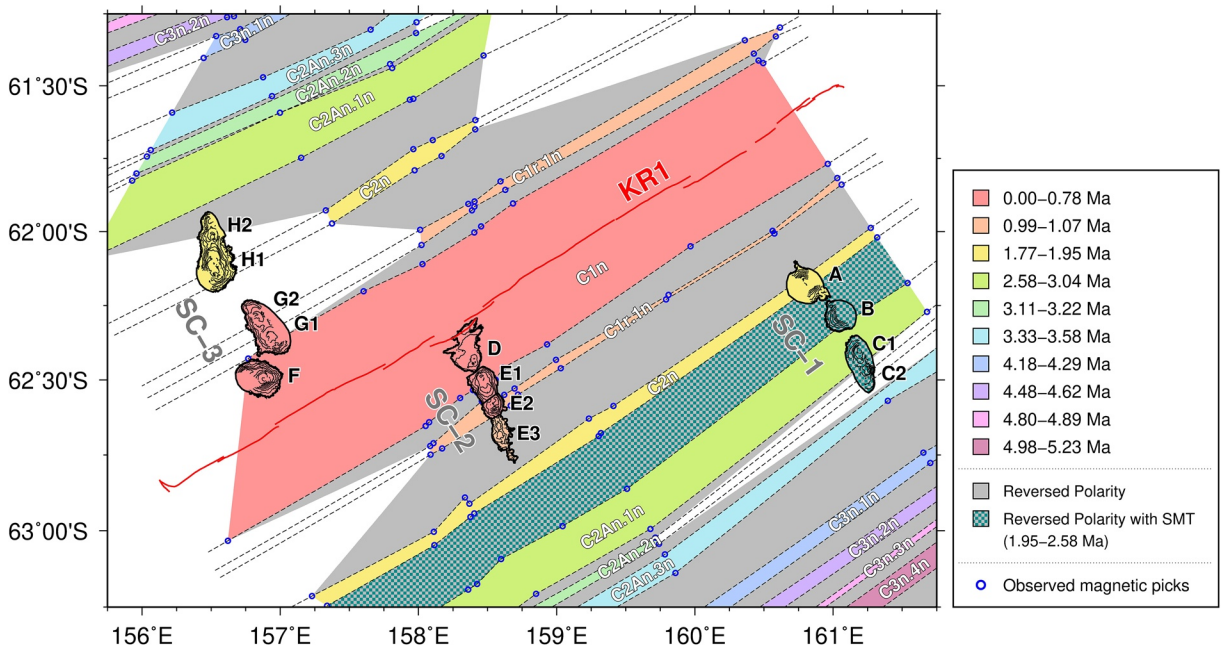

Figure 7. Spatial and temporal distribution of the seafloor and seamounts based on magnetic observations at segment KR1. The magnetic ages of the seamounts are indicated by the color gradation based on the corresponding location of the summit for each volcanic edifice. The magnetic picks marked with blue circles were determined from Choi et al. (2017) and this study.

4. Discussion

Geochemical dating of rock samples obtained from volcanic edifices is the most traditional method for determining seamount age (e.g., Davis et al., 2002; Geldmacher et al., 2000, 2005; Jackson et al., 1972; Sager & Pringle, 1987). Such age dating, however, tends to represent only the recent volcanic events (Hwang & Kim, 2016; Maia et al., 2005) because rock samples for age analyses are dredged from the seamount surface. The small off-axis seamounts appear to form through relatively rapid building processes (less than 1 Myr) (Jackson et al., 1972; Maia et al., 2005). The differences in the magnetization polarities between the seamounts and seafloor can be thus utilized to constrain the timing of off-axis volcanic formations (Maia et al., 2005).

The 2-D magnetic modeling approach used in this study relies on discrepancies between the observed and predicted seafloor magnetic anomalies, resulting from the nonsynchronous formation of seamounts and the underlying seafloor. As seen from seamounts B and H1, it may not be practical to distinguish any subtle discrepancies even if these existed. Moreover, some discrepancies could not be resolved by adjusting the geomagnetic polarity sequence alone (e.g., seamount D). For such cases, we make a conservative estimate by limiting the seamount formation time to the seafloor age.

The magnetic anomalies also can be modulated by the anomalous skewness of magnetization intensity. The value of anomalous skewness has been estimated as approximately 15–20° for an intermediate-spreading ridge and becomes negligible for fast-spreading ridges (half-spreading rates >~50 mm/yr) (Dyment & Arkani-Hamed, 1995; Koivisto et al., 2011). However, such asymmetry is known to generally depend on the orientation of lithospheric magnetization, not that of seamount magnetization (Dyment & Arkani-Hamed, 1995; Maia et al., 2005). The available data for this study could not investigate such depth-varying skewness in the magnetization intensity. Furthermore, we were only concerned in estimating the geomagnetic polarity sequence for seamounts, which is relatively less sensitive to such depth-dependent variation of magnetization intensity (Maia et al., 2005).

The magnetically constrained periods of the seamount formation in this study suggest that all the examined KR1 seamounts were formed within the last 3 Myrs (Figures 7 and 8a). Our analysis further shows that each seamount was formed over a period of less than 1 Myrs (Figures 7 and 8a; Table 1), and these can

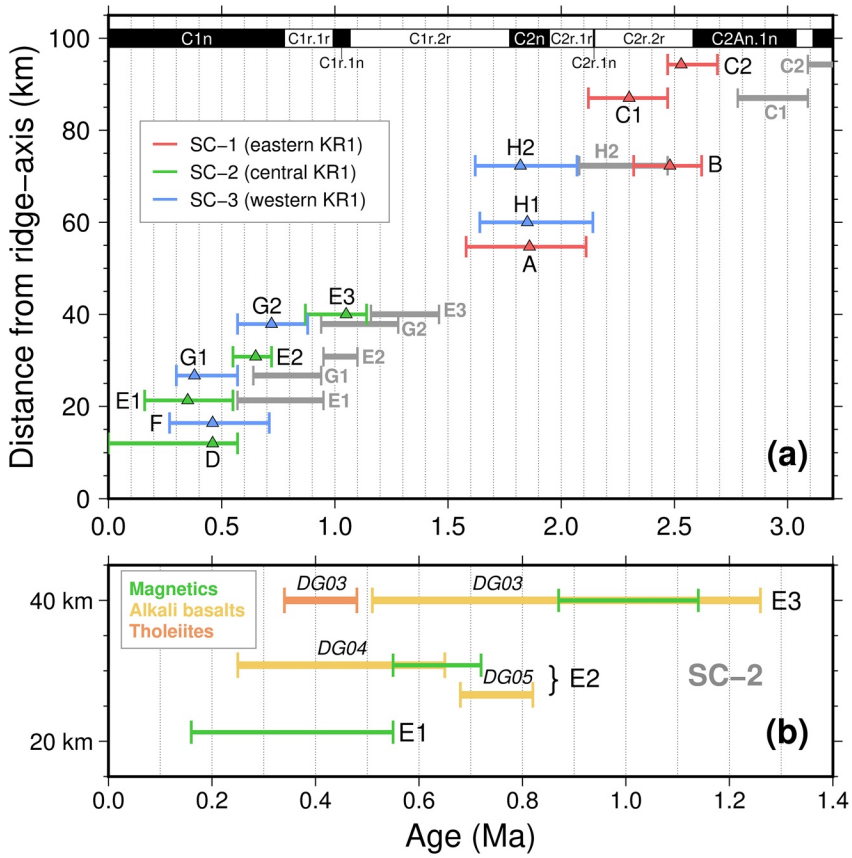

Figure 8. (a) Time and duration of volcanic eruptions as a function of seamount age versus distance from the ridge axis. The colored horizontal scale bars indicate the time of the volcanic eruption, and these data were adjusted from the initial model denoted by gray horizontal scale bars. The triangles show the location of the representative summit of each seamount. Red, green, and blue represent the seamounts in the eastern, central, and western KR1, respectively. (b) Comparison of the magnetically constrained seamount ages in this study with the radiogenic (e.g., [U-Th]/He and K-Ar) ages of the basalt samples from seamounts E2 and E3 (Yi et al., 2020).

be classified as a volcano with a fast-building process (Jackson et al., 1972; Maia et al., 2005). The longest formation time was identified from the seamount E group, that is, ~830 kyrs (e.g., seamount E1 formed during 0.16–0.55 Ma, E2 during 0.55–0.72 Ma, and E3 during 0.87–1.14 Ma), whereas the other seamounts exhibited formation times of less than 600 kyrs (Figure 8a and Table 1). For example, seamount A, the tallest edifice (~1.6 km tall) in segment KR1, required ~530 kyrs for its formation processes, whereas seamount H1, the most voluminous (~131 km^3) (Choi et al., 2021), was formed within ~500 kyrs (Figure 8a and Table 1). The duration of seamount formation was estimated by projecting the basal width of a given seamount to the adjusted or seafloor geomagnetic polarity sequence (e.g., Figure 4), assuming that the seamount formation occurred progressively with seafloor spreading. Our assumption may not hold true for all seamounts. However, the topographic width of any given seamount did not encompass a wide range of geomagnetic polarity sequences (Figures 4, 5 and 6). For example, seamount A is situated at the center of magnetic anomaly 2 according to the seafloor spreading model (Figure 4). If seamount A was entirely formed during magnetic anomaly 2, the estimated formation period based on its topographic width was longer than expected. Thus, our assumption on the progressive formation of seamounts may have overestimated the seamount formation period, thereby implying that the KR1 seamount formation periods could be shorter than the estimated.

Figure 8b shows a comparison of the seamount ages constrained by this study with the radiogenic ages for the basalt lavas dredged from seamounts E2 and E3 (Yi et al., 2020). The geomagnetic ages of seamounts E2 and E3 overlapped with the given uncertainty of radiogenic ages (Figure 8b). Although this comparison was limited to seamounts E2 and E3, the correlation between the magnetic and radiogenic dating for the

given seamounts suggests that our approach by adjusting the geomagnetic polarity sequence if needed was effective in determining the seamount formation periods.

The SC-1 seamounts located on the eastern KR1 contain the oldest off-axis seamounts of the B and C groups (Figure 8a). Then, the seamounts in the A (SC-1) and H group (SC-3; western KR1) were simultaneously formed. After a pause of ~440 kyrs in off-axis volcanism, seamount E3 was formed in the central KR1. Finally, recent volcanism occurred intensively in the western and central KR1 sections (Figure 8a). It is unclear whether such temporal and spatial variations in off-axis volcanism were correlated with the migration pattern of the melt supply along segment KR1 (e.g., Davis & Karsten, 1986). Nonetheless, the off-axis seamounts in the SC-1 on the eastern KR1 were likely associated with the previous excessive magma supply, because the present ridge morphology exhibits the rift valley and hence implies a poor magma supply.

Off-axis seamounts can be formed at a distance from the ridge axis if an excessive magma supply is available because axial melts prefer to feed volcanic eruptions at ridges. As a result, asymmetric off-axis seamount chains along the axis are commonly observed (Clague et al., 2000; Coumans et al., 2015; Katz et al., 2006; Scheirer & Macdonald, 1995). For example, the northern EPR, with full-spreading rates of ~80–120 mm/yr, exhibits off-axis seamounts formed within 5–15 km from the corresponding axes (Alexander & Macdonald, 1996; Scheirer & Macdonald, 1995). The spatial distribution of KR1 seamounts appears to be consistent with the northern EPR seamounts, as the KR1 seamounts were formed between 10 and 20 km from the axis. Although the distance gap between off-axis seamount formation and the axis is similar to that of the northern EPR system, the thermal and mechanical structures of segment KR1 are not favorable for EPR-type seamount production (Alexander & Macdonald, 1996; Rapparport et al., 1997; Scheirer & Macdonald, 1995). Considering the difference in spreading rates between the northern EPR and segment KR1, the oceanic lithosphere of segment KR1 is much thicker and colder than that of the northern EPR for the same distance offset from the axis. Following Bodine et al. (1981) and Calmant et al. (1990), the lithospheric thickness beneath the KR1 seamounts at a given off-axis distance are systematically thicker (~500 m on average) than those of the northern EPR. Although the seamount C group was formed at a ~20 km distance from the KR1 axis, it is inherently difficult to consider the seamount C group as a volcanic construct originated from an excessive magma supply near the ridge.

Apart from the excessive magma supply near the ridge crest, off-axis volcanism can be initiated by small-scale upwelling mediated by mantle heterogeneity (Davis & Karsten, 1986; Fornari et al., 1988; Harmon et al., 2011; Wilson, 1992). The Lamont seamounts located at ~8 km away from the northern EPR formed a ~50-km-long chain, for example, and these are regarded as volcanic formations originated from a primitive heterogeneous mantle source with depleted incompatible elements (Fornari et al., 1988). Moreover, the asymmetric distributions of off-axis seamounts at the JFR have been attributed to seafloor manifestations from the migration of the ridge-crest over a heterogeneous asthenosphere (Davis & Karsten, 1986). Nonetheless, both examples do not require a steady-state upwelling system associated with excessive near-ridge melting.

In particular, the off-axis seamount volcanism on the flanks along the JFR exhibits similar features with the KR1 seamounts. The JFR off-axis volcanism appears to have been initiated at ~20 km off-axis (i.e., ~0.7 Ma seafloor) and formed a ~60-km-long seamount chain (Davis & Karsten, 1986). Similarly, the seamount C group in this study was formed at ~20 km distance from the ridge axis (i.e., ~0.65 Ma seafloor) and consisted of a ~60-km-long seamount chain, that is, SC-1. Davis and Karsten (1986) suggested that the farther seamounts were formed away from the ridge axis, as more alkali basalts originating from the primitive melts with a lower fraction were present, whereas the closer seamounts from the axis were associated with more tholeiitic basalts originating from the evolved/mixed melts with a higher fraction (Davis & Karsten, 1986). Such petrological predictions as a function of distance from ridge axis is somewhat consistent with the recent geochemical results from the 8°20′N near-axis seamount chain in the EPR (Anderson et al., 2021).

Although there are no rock samples from the SC-1 seamounts to test the petrological prediction on off-axis volcanism (Davis & Karsten, 1986), the alkali basalts from seamounts E2 and E3 formed at ~10 km off-axis exhibit radiogenic Pb and mildly enriched Sr and Nd isotopic compositions (Yi et al., 2019, 2020). The radiogenic and isotopic enrichments observed at SC-2 might have originated from a magma source that reflects a small degree of partial melting with a lower fraction of heavy isotopes (e.g., Davis & Karsten, 1986). It is also

possible that the on-axis decompression melting would contribute to seamount E3 because of its close distance to the ridge axis (Anderson et al., 2021). Such melting heterogeneity of the upper mantle could have caused thermal instabilities and/or melt buoyancy and hence produced small-scale upwelling of melting on the young lithosphere at off-axis distances (Davis & Karsten, 1986; Fornari et al., 1988; Harmon et al., 2011; Katz et al., 2006; Wilson, 1992), which we consider as a plausible tectonic cause for the KR1 seamounts. More geochemical data are needed to assess the degree of heterogeneities of the sub-ridge upper mantle in this area (Anderson et al., 2021).

Park et al. (2019) established a new "Zealandia-Antarctic" mantle domain between the Pacific and Indian mantle domains, which might have originated from a super plume responsible for the Gondwana break-up at ~90 Ma. Considering that the regions have experienced a wide range of volcanism, the seismic tomography models of the proposed Zealandia-Antarctic mantle domain consistently illustrate a relatively hot upper mantle compared to the adjacent mantles (French et al., 2013; Koelemeijer et al., 2016; Langmuir et al., 1992; Park et al., 2019; Ritsema et al., 2011). Based on the isotopic compositions of Sr, Nd, Hf, and Pb from the KR1 and KR2 segments (see inset in Figure 1), Park et al. (2019) suggested that mixing between the plume components from the Balleny/Ross Island plume and depleted asthenosphere may have occurred in the vicinity of segment KR1. Such a geodynamic nature of the Zealandia-Antarctic mantle domain may have enhanced or impeded the off-axis volcanism in the study area, and further tests with more geophysical and geochemical samplings along the off-axis seamounts will be required for a thorough understanding.

5. Conclusions

We magnetically constrained the formation periods of the off-axis seamounts on the flanks of KR1, the easternmost segment of the Australian-Antarctic Ridge.

1. Based on the geomagnetically dated ages of the KR1 seamounts, all the isolated volcanic structures appear to have formed within the last ~3 Myrs, generally over a period of ~600 kyrs. Two major pulses of seamount volcanism were identified at 0.16–1.14 and 1.58–2.69 Ma, and these findings indicated there was a pause in seamount volcanism of approximately ~440 kyrs in the study area.
2. The 2-D magnetic modeling approach was effective in constraining the off-axis seamount formation period in the vicinity of segment KR1. As the magnetic anomalies were collected along the lines parallel to seafloor spreading and crossing the central seamounts, the MODMAG tool was suitable for determining the geomagnetic polarity sequence for the seamounts.
3. The off-axis seamounts in segment KR1 were formed with a temporal gap of 200–650 kyrs from their underlying seafloor formation and at 10–20 km distance from the KR1 axis. Typically, off-axis seamounts are associated with an excessive magma supply originated from large-scale axial upwelling. However, the thermal and mechanical properties of the intermediate-spreading lithospheric system at segment KR1 were not supportive of such an excessive axial magma supply. However, fertile melting heterogeneity of the upper mantle could offer a better explanation for the KR1 off-axis seamounts, with support provided by the enrichments in radiogenic and isotopic compositions of the rock samples.

Data Availability Statement

The data sets used for this study are available from the Korea Polar Data Center (KPDC) (https://dx.doi.org/doi:10.22663/KOPRI-KPDC-00001677.2).

Acknowledgments
The authors thank the captains and crew of the R/VIB *Araon* for their efforts during the expeditions. This study was supported by the Korea Polar Research Institute, under grant numbers PE21050 and PE20210. S.-S. Kim acknowledges support from the National Research Foundation of Korea (NRF) (NRF-2017R1D1A1A02018632 and NRF-2021R1A2C1012030). The authors would like to thank four anonymous reviewers, Fabio Caratori Tontini, the Associate Editor, and the Editor Claudio Faccenna for critically reading the manuscript and suggesting substantial improvements.

References

Alexander, R. T., & Macdonald, K. C. (1996). Small off-axis volcanoes on the East Pacific Rise. *Earth and Planetary Science Letters*, *139*(3–4), 387–394. https://doi.org/10.1016/0012-821X(96)00028-3

Anderson, M., Wanless, V. D., Perfit, M., Conrad, E., Gregg, P., Fornari, D., & Ridley, W. I. (2021). Extreme heterogeneity in mid-ocean ridge mantle revealed in lavas from the 8°20′N near-axis seamount chain. *Geochemistry, Geophysics, Geosystems*, *22*(1). https://doi.org/10.1029/2020GC009322

Batiza, R. (1982). Abundances, distribution and sizes of volcanoes in the Pacific Ocean and implications for the origin of non-hotspot volcanoes. *Earth and Planetary Science Letters*, *60*(2), 195–206. https://doi.org/10.1016/0012-821X(82)90003-6

Blakely, R. J. (1995). *Potential theory in gravity and magnetics applications* (1st ed.). Cambridge University Press. https://doi.org/10.1017/CBO9780511549816

Bodine, J. H., Steckler, M. S., & Watts, A. B. (1981). Observations of flexure and the rheology of the oceanic lithosphere. *Journal of Geophysical Research*, *86*(B5), 3695–3707. https://doi.org/10.1029/JB086iB05p03695

Briais, A., Ondréas, H., Klingelhoefer, F., Dosso, L., Hamelin, C., & Guillou, H. (2009). Origin of volcanism on the flanks of the Pacific-Antarctic Ridge between 41°30′S and 52°S. *Geochemistry, Geophysics, Geosystems*, *10*(9). https://doi.org/10.1029/2008GC002350

Calmant, S. (1987). The elastic thickness of the lithosphere in the Pacific Ocean. *Earth and Planetary Science Letters*, *85*(1–3), 277–288. https://doi.org/10.1016/0012-821X(87)90038-0

Calmant, S., Francheteau, F., & Cazenave, A. (1990). Elastic layer thickening with age of the oceanic lithosphere: A tool for prediction of the age of volcanoes or oceanic crust. *Geophysical Journal International*, *100*(1), 59–67. https://doi.org/10.1111/j.1365-246X.1990.tb04567.x

Cande, S. C., & Kent, D. V. (1995). Revised calibration of the geomagnetic polarity timescale for the Late Cretaceous and Cenozoic. *Journal of Geophysical Research*, *100*(B4), 6093–6095. https://doi.org/10.1029/94JB03098

Caratori Tontini, F., Cocchi, L., & Carmisciano, C. (2008). Potential-field inversion for a layer with uneven thickness: The Tyrrhenian Sea density model. *Physics of the Earth and Planetary Interiors*, *166*(1–2), 105–111. https://doi.org/10.1016/j.pepi.2007.10.007

Choi, H., Kim, S.-S., Dyment, J., Granot, R., Park, S.-H., & Hong, J. K. (2017). The kinematic evolution of the Macquarie Plate: A case study for the fragmentation of oceanic lithosphere. *Earth and Planetary Science Letters*, *478*, 132–142. https://doi.org/10.1016/j.epsl.2017.08.035

Choi, H., Kim, S.-S., & Park, S.-H. (2013). Interpretation of bathymetric and magnetic data from the easternmost segment of Australian-Antarctic Ridge, 156°–161°E (Vol. 2013, pp. T13A–T2498). American Geophysical Union Fall Meeting Abstracts.

Choi, H., Kim, S.-S., Park, S.-H., & Kim, H. J. (2021). Geomorphological and spatial characteristics of underwater volcanoes in the easternmost Australian-Antarctic Ridge. *Remote Sensing*, *13*(5), 997. https://doi.org/10.3390/rs13050997

Christie, D. M., West, B. P., Pyle, D. G., & Hanan, B. B. (1998). Chaotic topography, mantle flow and mantle migration in the Australian-Antarctic discordance. *Nature*, *394*(6694), 637–644. https://doi.org/10.1038/29226

Clague, D. A., Reynolds, J. R., & Davis, A. S. (2000). Near-ridge seamount chains in the northeastern Pacific Ocean. *Journal of Geophysical Research*, *105*(B7), 16541–16561. https://doi.org/10.1029/2000JB900082

Clouard, V., & Bonneville, A. (2005). Ages of seamounts, islands, and plateaus on the Pacific plate. In G. R. Foulger, J. H. Natland, D. C. Presnall, & D. L. Anderson (Eds.), *Plates, plumes and paradigms*. Geological Society of America. https://doi.org/10.1130/0-8137-2388-4.71

Coumans, J. P., Stix, J., Clague, D. A., & Minarik, W. G. (2015). The magmatic architecture of Taney seamount-A, NE Pacific Ocean. *Journal of Petrology*, *56*(6), 1037–1067. https://doi.org/10.1093/petrology/egv027

Davis, A. S., Gray, L. B., Clague, D. A., & Hein, J. R. (2002). The Line Islands revisited: New $^{40}Ar/^{39}Ar$ geochronologic evidence for episodes of volcanism due to lithospheric extension. *Geochemistry, Geophysics, Geosystems*, *3*, 1–28. https://doi.org/10.1029/2001GC000190

Davis, E. E., & Karsten, J. L. (1986). On the cause of the asymmetric distribution of seamounts about the Juan de Fuca ridge: Ridge-crest migration over a heterogeneous asthenosphere. *Earth and Planetary Science Letters*, *79*, 385–396. https://doi.org/10.1016/0012-821X(86)90194-9

DeMets, C., Gordon, R. G., & Argus, D. F. (2010). Geologically current plate motions. *Geophysical Journal International*, *181*(1), 1–80. https://doi.org/10.1111/j.1365-246X.2009.04491.x

Dick, H. J. B., Lin, J., & Schouten, H. (2003). An ultraslow-spreading class of ocean ridge. *Nature*, *426*(6965), 405–412. https://doi.org/10.1038/nature02128

Dyment, J., & Arkani-Hamed, J. (1995). Spreading-rate-dependent magnetization of the oceanic lithosphere inferred from the anomalous skewness of marine magnetic anomalies. *Geophysical Journal International*, *121*, 789–804. https://doi.org/10.1111/j.1365-246X.1995.tb06439.x

Fabbrizzi, A., Parnell-Turner, R., Gregg, P., Fornari, D., Perfit, M., Wanless, D., & Anderson, M. (2020). *Dating off-axis volcanism on 8°20′N seamounts using sediment thickness from near-bottom chirp*. AGU Fall Meeting Abstracts. V040-002.

Fornari, D. J., Perfit, M. R., Allan, J. F., Batiza, R., Haymon, R., Barone, A., et al. (1988). Geochemical and structural studies of the Lamont seamounts: Seamounts as indicators of mantle processes. *Earth and Planetary Science Letters*, *89*, 63–83. https://doi.org/10.1016/0012-821X(88)90033-7

French, S., Lekic, V., & Romanowicz, B. (2013). Waveform tomography reveals channeled flow at the base of the oceanic asthenosphere. *Science*, *342*, 227–230. https://doi.org/10.1126/science.1241514

Gee, J., Staudigel, H., Tauxe, L., Pick, T., & Gallet, Y. (1993). Magnetization of the La Palma Seamount Series: Implications for seamount paleopoles. *Journal of Geophysical Research: Solid Earth*, *98*(B7), 11743–11767. https://doi.org/10.1029/93JB00932

Geldmacher, J. P., Hoernle, K., van den Bogaard, P., Duggen, S., & Werner, R. (2005). New $^{40}Ar/^{39}Ar$ age and geochemical data from seamounts in the Canary and Madeira volcanic provinces: Support for the mantle plume hypothesis. *Earth and Planetary Science Letters*, *237*, 85–101. https://doi.org/10.1016/j.epsl.2005.04.037

Geldmacher, J. P., van den Bogaard, P., Hoernle, K., & Schmincke, H.-U. (2000). The $^{40}Ar/^{39}Ar$ age dating of the Madeira Archipelago and hotspot track (eastern North Atlantic). *Geochemistry, Geophysics, Geosystems*, *1*, 1–26. https://doi.org/10.1029/1999GC000018

Hahm, D., Baker, E. T., Rhee, T. S., Won, Y.-J., Resing, J. A., Lupton, J. E., et al. (2015). First hydrothermal discoveries on the Australian-Antarctic Ridge: Discharge sites, plume chemistry, and vent organisms. *Geochemistry, Geophysics, Geosystems*, *16*(9), 3061–3075. https://doi.org/10.1002/2015GC005926

Hanan, B. B., Blichert-Toft, J., Pyle, D. G., & Christie, D. M. (2004). Contrasting origins of the upper mantle revealed by hafnium and lead isotopes from the Southeast Indian Ridge. *Nature*, *432*(7013), 91–94. https://doi.org/10.1038/nature03026

Harmon, N., Forsyth, D. W., Weeraratne, D. S., Yang, Y., & Webb, S. C. (2011). Mantle heterogeneity and off axis volcanism on young Pacific lithosphere. *Earth and Planetary Science Letters*, *311*, 306–315. https://doi.org/10.1016/j.epsl.2011.09.038

Hillier, J. K. (2007). Pacific seamount volcanism in space and time. *Geophysical Journal International*, *168*(2), 877–889. https://doi.org/10.1111/j.1365-246X.2006.03250.x

Hwang, G., & Kim, S.-S. (2016). Flexure and gravity anomalies of the oceanic lithosphere beneath the Louisville seamount. *Tectonophysics*, *686*, 19–26. https://doi.org/10.1016/j.tecto.2016.07.014

Ito, G., & Behn, M. D. (2008). Magmatic and tectonic extension at mid-ocean ridges: 2. Origin of axial morphology. *Geochemistry, Geophysics, Geosystems*, *9*, 1–20. https://doi.org/10.1029/2008GC001970

Jackson, E. D., Silver, E. A., & Dalrymple, G. B. (1972). Hawaiian-Emperor chain and its relations to Cenozoic Pacific tectonics. *Geological Society America Bulletin*, *83*(3), 601–618. https://doi.org/10.1130/0016-7606(1972)83[601:HCAIRT]2.0.CO;2

Katz, R. F., Spiegelman, M., & Holtzman, B. (2006). The dynamics of melt and shear localization in partially molten aggregates. *Nature*, *442*(7103), 676–679. https://doi.org/10.1038/nature05039

Kim, S.-S., Lin, J., Park, S.-H., & Choi, H. (2015). *Geophysical investigation of Australian-Antarctic Ridge using high-resolution gravity and bathymetry* (pp. DI51B–2628). American Geophysical Union Fall Meeting Abstracts.
Kim, S.-S., & Wessel, P. (2010). Flexure modelling at seamounts with dense cores: Flexure modelling with dense core loads. *Geophysical Journal International*, *182*(2), 583–598. https://doi.org/10.1111/j.1365-246X.2010.04653.x
Kim, S.-S., & Wessel, P. (2011). New global seamount census from altimetry-derived gravity data. *Geophysical Journal International*, *186*(2), 615–631. https://doi.org/10.1111/j.1365-246X.2011.05076.x
Klein, E. M., Langmuir, C. H., Zindler, A., Staudigel, H., & Hamelin, B. (1988). Isotope evidence of a mantle convection boundary at the Australian-Antarctic Discordance. *Nature*, *333*(6174), 623–629. https://doi.org/10.1038/333623a0
Koelemeijer, P., Ritsema, J., Deuss, A., & van Heijst, H.-J. (2016). SP12RTS: A degree-12 model of shear- and compressional-wave velocity for Earth's mantle. *Geophysical Journal International*, *204*, 1024–1039. https://doi.org/10.1093/gji/ggv481
Koivisto, E. A., Gordon, R. G., Dyment, J., & Arkani-Hamed, J. (2011). The spreading-rate dependence of anomalous skewness of Pacific plate magnetic anomaly 31: Revisited. *Lithosphere*, *3*, 371–378. https://doi.org/10.1130/L167.1
Koppers, A. A. P., & Watts, A. (2010). Intraplate seamounts as a window into deep Earth processes. *Oceanography*, *23*(1), 42–57. https://doi.org/10.5670/oceanog.2010.61
Koppers, A. A. P., Yamazaki, T., Geldmacher, J., Gee, J. S., Pressling, N., Koppers, A. A. P., et al. (2012). Limited latitudinal mantle plume motion for the Louisville hotspot. *Nature Geoscience*, *5*(12), 911–917. https://doi.org/10.1038/ngeo1638
Langmuir, C. H., Klein, E. M., & Plank, T. (1992). Mantle flow and melt generation beneath ocean ridges. In J. P. Morgan, D. K. Blackman, & J. M. Sinton (Eds.), Geophysical monograph series (Vol. 71, pp. 183–280). American Geophysical Union.
Macdonald, K. C. (2001). Mid-ocean ridge tectonics, volcanism, and geomorphology. In J. Steele, S. Thorpe, & K. Turekian (Eds.), *Encyclopedia of ocean sciences* (pp. 1798–1813). Academic Press. https://doi.org/10.1006/rwos.2001.0094
Macrì, P., Sagnotti, L., Dinarès-Turell, J., & Caburlotto, A. (2010). Relative geomagnetic paleointensity of the Brunhes Chron and the Matuyama-Brunhes precursor as recorded in sediment core from Wilkes Land Basin (Antarctica). *Physics of the Earth and Planetary Interiors*, *179*, 72–86. https://doi.org/10.1016/j.pepi.2009.12.002
Maia, M., Dyment, J., & Jouannetaud, D. (2005). Constraints on age and construction process of the Foundation chain submarine volcanoes from magnetic modeling. *Earth and Planetary Science Letters*, *235*(1–2), 183–199. https://doi.org/10.1016/j.epsl.2005.02.044
Mendel, V., Munschy, M., & Sauter, D. (2005). MODMAG, a MATLAB program to model marine magnetic anomalies. *Computers & Geosciences*, *31*(5), 589–597. https://doi.org/10.1016/j.cageo.2004.11.007
Park, S.-H., Langmuir, C. H., Lin, J., Kim, S.-S., Hahm, D., Michael, P. J., et al. (2014). *Mantle domain and segmentation at the Australian-Antarctic Ridge*. American Geophysical Union Fall Meeting Abstracts. OS53C-1055.
Park, S.-H., Langmuir, C. H., Sims, K. W. W., Blichert-Toft, J., Kim, S.-S., Scott, S. R., et al. (2019). An isotopically distinct Zealandia-Antarctic mantle domain in the Southern Ocean. *Nature Geoscience*, *12*(3), 206–214. https://doi.org/10.1038/s41561-018-0292-4
Parker, R. L. (1973). The rapid calculation of potential anomalies. *Geophysical Journal International*, *31*(4), 447–455. https://doi.org/10.1111/j.1365-246X.1973.tb06513.x
Parker, R. L. (1988). A statistical theory of seamount magnetism. *Journal of Geophysical Research*, *93*(B4), 3105–3115. https://doi.org/10.1029/JB093iB04p03105
Parker, R. L. (1991). A theory of ideal bodies for seamount magnetism. *Journal of Geophysical Research*, *96*(B10), 16101–16112. https://doi.org/10.1029/91JB01497
Parker, R. L., & Huestis, S. P. (1974). The inversion of magnetic anomalies in the presence of topography. *Journal of Geophysical Research*, *79*(11), 1587–1593. https://doi.org/10.1029/JB079i011p01587
Parker, R. L., Shure, L., & Hildebrand, J. A. (1987). The application of inverse theory to seamount magnetism. *Reviews of Geophysics*, *25*, 17–40. https://doi.org/10.1029/RG025i001p00017
Parsons, B., & Sclater, J. G. (1977). An analysis of the variation of ocean floor bathymetry and heat flow with age. *Journal of Geophysical Research*, *82*, 803–827. https://doi.org/10.1029/JB082i005p00803
Phipps Morgan, J., & Chen, Y. (1993). Dependence of ridge-axis morphology on magma supply and spreading rate. *Nature*, *364*, 706–708. https://doi.org/10.1038/364706a0
Rapparport, Y., Naar, D. F., Barton, C. C., Liu, Z. J., & Hey, R. N. (1997). Morphology and distribution of seamounts surrounding Easter Island. *Journal of Geophysical Research*, *102*(B11), 24713–24728. https://doi.org/10.1029/97JB01634
Reynolds, J. R., & Langmuir, C. H. (2000). Identification and implications of off-axis lava flows around the East Pacific Rise. *Geochemistry, Geophysics, Geosystems*, *1*(6). https://doi.org/10.1029/1999GC000033
Ritsema, J., Deuss, A., van Heijst, H. J., & Woodhouse, J. H. (2011). S40RTS: A degree-40 shear-velocity model for the mantle from new Rayleigh wave dispersion, teleseismic travel time and normal-mode splitting function measurements. *Geophysical Journal International*, *184*, 1223–1236. https://doi.org/10.1111/j.1365-246X.2010.04884.x
Sager, W., & Pringle, M. S. (1987). Paleomagnetic constraints on the origin and evolution of the Musicians and South Hawaiian seamounts, central Pacific Ocean. In B. H. Keating, P. Fryer, R. Batiza, & W. W. Boehlert (Eds.), *Seamounts, Islands and Atolls, Geophysical Monograph* (pp. 133–162). American Geophysical Union. https://doi.org/10.1029/GM043p0133
Sager, W. W., & Pringle, M. S. (1990). Paleomagnetic evidence for Cretaceous age of two volcanoes on the south flank of the Island of Hawaii. *Geophysical Research Letters*, *17*(13), 2445–2448. https://doi.org/10.1029/GL017i013p02445
Scheirer, D. S., & Macdonald, K. C. (1995). Near-axis seamounts on the flanks of the East Pacific Rise, 8°N to 17°N. *Journal of Geophysical Research*, *100*(B2), 2239–2259. https://doi.org/10.1029/94JB02769
Schouten, H., Tivey, M. A., Fornari, D. J., & Cochran, J. R. (1999). Central anomaly magnetization high: Constraints on the volcanic construction and architecture of seismic layer 2A at a fast-spreading mid-ocean ridge, the EPR at 9°30′–50′N. *Earth and Planetary Science Letters*, *169*, 37–50. https://doi.org/10.1016/S0012-821X(99)00063-1
Smith, D. K., & Cann, J. R. (1992). The role of seamount volcanism in crustal construction at the Mid-Atlantic Ridge (24°–30°N). *Journal of Geophysical Research*, *97*(B2), 1645–1658. https://doi.org/10.1029/91JB02507
Smith, W. H. F., & Sandwell, D. T. (1997). Global seafloor topography from satellite altimetry and ship depth soundings. *Science*, *277*(5334), 1957–1962. https://doi.org/10.1126/science.277.5334.1956
Supak, S., Carbotte, S. M., & Macdonald, K. C. (2007). Influence of ridge migration and proximity to hot spots on the morphology of slow- and intermediate-spreading centers. *Geochemistry, Geophysics, Geosystems*, *8*(1). https://doi.org/10.1029/2006GC001387
Thébault, E., Finlay, C., Beggan, C., Alken, P., Aubert, J., Barrois, O., et al. (2015). International geomagnetic reference field: The 12th generation. *Earth, Planets and Space*, *67*(1), 79. https://doi.org/10.1186/s40623-015-0228-9
Watts, A. B., Sandwell, D. T., Smith, W. H. F., & Wessel, P. (2006). Global gravity, bathymetry, and the distribution of submarine volcanism through space and time. *Journal of Geophysical Research*, *111*(B8). https://doi.org/10.1029/2005JB004083

Wessel, P. (1997). Sizes and ages of seamounts using remote sensing: Implications for intraplate volcanism. *Science*, *277*(5327), 802–805. https://doi.org/10.1126/science.277.5327.802

Wessel, P., Sandwell, D., & Kim, S.-S. (2010). The global seamount census. *Oceanography*, *23*(1), 24–33. https://doi.org/10.5670/oceanog.2010.60

White, S. M., Macdonald, K. C., Scheirer, D. S., & Cormier, M.-H. (1998). Distribution of isolated volcanoes of the flanks of the East Pacific Rise, 15.3°S–20°S. *Journal of Geophysical Research*, *103*, 30371–30384. https://doi.org/10.1029/98JB02791

Whittaker, J. M., Müller, R. D., & Gurnis, M. (2010). Development of the Australian-Antarctic depth anomaly. *Geochemistry, Geophysics, Geosystems*, *11*(11). https://doi.org/10.1029/2010GC003276

Wilson, D. S. (1992). Focused mantle upwelling beneath mid-ocean ridges: Evidence from seamount formation and isostatic compensation of topography. *Earth and Planetary Science Letters*, *113*, 41–55. https://doi.org/10.1016/0012-821X(92)90210-M

Yang, T., Hyodo, M., Yang, Z., & Fu, J. (2007). Two geomagnetic excursions during the Brunhes chron recorded in Chinese loess-palaeosol sediments. *Geophysical Journal International*, *171*, 104–114. https://doi.org/10.1111/j.1365-246X.2007.03522.x

Yi, S.-B., Lee, M.-J., Park, S.-H., Han, S., Yang, Y.-S., & Choi, H. (2019). Occurrence of ice-rafted erratics and the petrology of the KR1 seamount trail from the Australian-Antarctic Ridge. *International Geology Review*, *61*(12), 1429–1445. https://doi.org/10.1080/00206814.2018.1514669

Yi, S.-B., Lee, M.-J., Park, S.-H., Nagao, K., Han, S., Yang, Y.-S., et al. (2020). Alkalic to tholeiitic magmatism near a mid-ocean ridge: Petrogenesis of the KR1 Seamount Trail adjacent to the Australian-Antarctic Ridge. *International Geology Review*. https://doi.org/10.1080/00206814.2020.1756002

Zindler, A., Staudigel, H., & Batiza, R. (1984). Isotope and trace element geochemistry of young Pacific seamounts: Implications for the scale of upper mantle heterogeneity. *Earth and Planetary Science Letters*, *70*(2), 175–195. https://doi.org/10.1016/0012-821X(84)90004-9